Supporting Information

Balancing ion diffusion-reduction in chlorine-free electrolytes enables long-life Mg metal batteries

Juncai Long,[a] Yi Liu,[a] Wenwei Zhang,[a] Ge Zhang,[a] Pei Liu,[a] Lianmeng Cui,[a] Cheng Zhou,[a] Jingke Ren,[a] Ze He,[a,b] Qinyou An,*[a,c] and Liqiang Mai*[a,c]*

[a]State Key Laboratory of Advanced Technology for Materials Synthesis and Processing, Wuhan University of Technology, Wuhan 430070, P. R. China

[b]Institute for Manufacturing, Department of Engineering, University of Cambridge, Cambridge CB3 0FS, UK

[c]Hubei Longzhong Laboratory, Wuhan University of Technology (Xiangyang Demonstration Zone), Xiangyang 441000, P. R. China

* Corresponding Author: E-mail: He816414@163.com (Z. He); anqinyou86@whut.edu.cn (Q. An); mlq518@whut.edu.cn (L. Mai)

Reagents: All reagents were received from Sigma-Aldrich or Aladdin and used without further purification.

Electrolyte preparation: $Mg(HFIP)_2$ salts were synthesized according to previous report. [1] Briefly, in an argon filled glovebox, 1,1,1,3,3,3-Hexafluoro-2-propanol ($(CF_3)_2CHOH$, 22 mmol) was dissolved in 10 mL dry 1,2-dimethoxyethane (DME), then, add 10 ml of Di-n-butyl magnesium ($[CH_3(CH_2)_3]_2Mg$, 10 mmol, 1.0 M in heptane) solution slowly to the above solution and stir overnight, the reaction is violently exothermic. Finally, the solvent is removed in vacuum to obtain white powder, which is $Mg(HFIP)_2$ salt. Then, 20 mmol $Mg(HFIP)_2$ salts are added to the 10 mL DME solvent to form the transparent and stable solutions.

For tetrabutylammonium borohydride ($TBABH_4$) modified electrolyte, the 2M $Mg(HFIP)_2$ electrolyte with additive concentration of 20mM, 40mM, and 60 mM were prepared, respectively. The water content of electrolytes was approximately 2000 ppm, measured using a Coulometric Karl Fischer Moisture Meter (C20s).

Cathode preparation

Synthesis of Mo_6S_8 cathode: The Chevrel Mo_6S_8 was synthesized according to the previous work. [2] Briefly, 0.8 g CuS, 1.6 g MoS_2, 1.2 g Mo powder and 16 g KCl were mixed and ball milled at 350 rpm for 3 hours. The ground powder was then transferred to a crucible for sintering. Under a sealed argon atmosphere, the sample was sintered in a tubular furnace at 300 ˚C for 1 h, then, the sample was heated up to 1000 ˚C for another 24 h. After cooling to room temperature, the products were washed with deionized water and $CuMo_6S_8$ could be obtained. As prepared $CuMo_6S_8$ was then immersed into a 6 M HCl solution and stirred for 72

h. The solution was centrifuged and Mo_6S_8 precipitates were washed with deionized water and dried in vacuum at 80 ˚C. The Mo_6S_8 cathodes were prepared by spreading the mixed slurry composed of 70 wt% Mo_6S_8 powder, 20 wt% super P, and 10 wt% polyvinylidene fluoride (PVDF) in NMP solvent to stainless steel (SS) foils and dried at 70 ˚C. The mass loading of the active material is about 1-2 mg cm^{-2}.

Synthesis of P14AQ cathode: P14AQ was synthesized according to the previous work. [3] Typically, bis(1,5-cyclooctadiene)nickel(0) ($Ni(COD)_2$, 2.2 g, 8 mmol), 2,2'-bipyridine (1.25 g, 8 mmol), and 1,5-cyclooctadiene (COD, 0.74 ml, 6 mmol) were first dissolved in 60 mL dimethylformamide (DMF) in a Schlenk flask. 1,4-dichloroanthraquinone (1,4-DCAQ, 2.2 g, 8 mmol) was dissolved in 40 ml DMF and added into the above solution. These procedures were carried out in an argon-filled glove box (O_2, H_2O < 0.1 ppm). Subsequently, the polymerization reaction was carried out by heating the mixed solution at 60 ˚C for 48 h under argon using a Schlenk line in fume hood. Then the reaction mixture was poured into a beaker containing 150 ml, 0.5M hydrochloric acid solution. The yellow product precipitated immediately. Then it was filtered and washed with DMF, 0.5M hydrochloric acid, warm deionized water, and methanol for several times. Subsequently, it was purified by re-precipitation by dissolving the raw product in chloroform and adding methanol afterwards. Finally, the polymer material was further washed through Soxhlet extraction in DME for 48 h to remove the soluble short-chain polymer and dried at 80 ˚C for 12 h under vacuum. The P14AQ cathodes were obtained with 50 wt% P14AQ powder, 40 wt% ketjen black and 10 wt% PTFE. These three materials are mixed and moulded on a roller press. The loading of the active material was about 3–5 mg cm^{-2}.

Materials characterizations: Fourier transform infrared (FTIR) spectra were measured by using Nicolet iS50 FTIR spectrometer in diffuse reflectance mode. Raman spectra were obtained using a Renishaw INVIA micro-Raman spectroscopy system. X-ray photoelectron spectroscopy (XPS) measurements were carried out using Kratos Axis Supra XPS instrument. TOF-SIMS measurements were conducted with a ULVAC-PHI PHI nano TOF 3 instrument. JEOL-7100F microscope was utilized to collect scanning electron microscopy (SEM) images. Structural characterizations of the samples were performed on an X-ray diffractometer (XRD) in the detected angular range of $5^\circ < 2\theta < 80^\circ$ (D2 Advance, Cu Kα radiation, λ = 1.5418 Å). The morphologies were characterized using the three-dimensional (3D) laser scanning microscopy (LSM, KEYENCE VK-X1000) and in situ optical microscope. For the characterization of SEI, Mg||Mg symmetrical cells with different electrolytes were disassembled after 20 charge-discharge cycles at a current density of 0.1 mA cm^{-2}, 1 h charging and 1 h discharging. Then, the cycled Mg metal electrodes sample were rinsed with dry DME (3 times) in glove box.

Electrochemical measurement: CR2016 coin cells were assembled in an Ar-filled glove box with Mg metal foil as the anode, glass fiber membrane (GF/A What-man) as the separator. The electrochemical performance of the batteries was performed by using a multi-channel battery test system (NEWARE Battery Test System, Shenzhen, China, CT-4008-5V 10mA-164 and LAND CT2001A) at room temperature. CE measurements were conducted using asymmetric Mg||SS cells. The cells were discharged for 60 minutes and charge to 1.5 V at a current density of 0.5 mA cm^{-2}. Symmetric Mg||Mg cells were assembled for evaluating the polarization properties of the electrolyte. Cyclic voltammetry (CV) curves and linear scan voltammetry

(LSV) were tested using a BioLogic VMP3 multichannel electrochemical workstation. The CV was studied by a three-electrode system using Mg as the reference and counter electrode and SS as the working electrode at a scanning rate of 25 mV s^{-1}. LSV was carried out using SS foils as the working electrode and Mg foil as the reference and counter electrode. The scan rate was 10 mV s^{-1}. The EIS test was obtained at room temperature in the frequency from 0.01 Hz to 100000 Hz. Deposited Mg for SEM was obtained at a current density of 0.2 mA cm^{-2} (Higher than our previously work, cause a (002) plane-dominated Mg plating morphology is only observed at low current densities in blank $Mg(HFIP)_2$ electrolyte). [2] Mg foil employed had a thickness of 100 μm. The Mg plating current density during the in situ optical microscopy tests was 0.2 mA cm^{-2}.

Theoretical Calculation

DFT calculation: All density functional theory (DFT) calculations were carried out Vienna ab initio Simulation package (VASP).[4] Exchange-correlation interactions are determined by the Perdew-Burke-Ernzerhof (PBE) functional in the generalised gradient approach (GGA). The plane-wave cutoff energy was 500 eV. The convergence of energy and forces were set to 1×10^{-5} eV and 0.02 eV/Å, respectively. $1\times1\times1$ k-points were used to sample the Brillouin zone. The Grimme's dispersion correction method for DFT-D3 is used to account for the van der Waals (vdW) interactions2. [5] The (6×6) cells were constructed to model the Mg (002), (100) and (101) surface and a vacuum thickness of 15 Å was applied. The adsorption energies (E_{ads}) were calculated as $E_{ads}=E_{total}-E_{system}-E_{Mg}$, where E_{total}, E_{system}, and E_{Mg} are the total energy and the atomic energy of Mg adsorption by/without Mg atoms, respectively. Crystal structure diagrams were drawn with Visualization for Electronical and Structural Analysis (VESTA). [6]

The lattice mismatch is calculated using the following equation:

$$\frac{\Delta a}{a} = (a1 - a2)/a1$$

In this equation, Δa is the difference between the lattice constants of the two materials, *a1* and *a2* are the lattice constants of a set of crystals, respectively, with *a1* usually taken as a reference to the one with the larger value.

Lattice parameters of Mg metal:

a	*b*	*c*	*alpha*	*beta*	*gamma*
3.20940	*3.20940*	*5.21050*	*90.0000*	*90.0000*	*120.0000*

Unit-cell volume = 46.479098 Å^3

Finite Element Method Simulations: The ion transport for the magnesian anode was predicted with a 3D Nernst-Planck formulation accounting for diffusion and migration in the bulk electrolyte. The modeling domain, geometrical dimensions, and major boundary conditions are shown in Figure 3. The governing equations for magnesian anode were given as:

$$\nabla^2\varphi = -F\sum z_{\mathrm{i}}C_{\mathrm{i}}$$
$$\frac{\partial C_{\mathrm{i}}}{\partial \mathrm{t}} = \nabla\cdot\left[D_{\mathrm{i}}\nabla C_{\mathrm{i}} + \frac{D_{\mathrm{i}}C_{\mathrm{i}}}{\mathrm{RT}}z_{\mathrm{i}}\nabla\varphi\right]$$

where *F*, *R* and *T* are the Faraday constant, ideal gas constant and temperature, D_i is the initial diffusion coefficient (1×10^{-10} m^2 /s for Mg^{2+} DOI: 10.1073/pnas.2111549118), *ci* is the ion concertation, *zi* is the charge number, and φ is the electrolyte potential. Electroneutrality was assumed throughout the whole domains. In the experiment, the flux of magnesian ion is uniform

through the 3D structure. The experimental current is 1mA cm^{-2}, the electrode length and width all are 4 microns, and the overall diffusion distance of electrolyte is 4 microns. Firstly, considering the situation without additives, a model with the initial structure is established to obtain the electric field distribution. Here, the evolution of electric field distribution is shown in Figure3. The model the processed electrochemistry model was imported into the finite element software COMSOL® (Stockholm, Sweden), where the material properties were defined and the relevant problems were calculated and analyzed. To solve the discretized transport and electrode deformation kinematics equations, the Parallel Direct Sparse Solver (PARDISO) was employed. Time stepping was handled using 2nd order backward Euler differentiation.

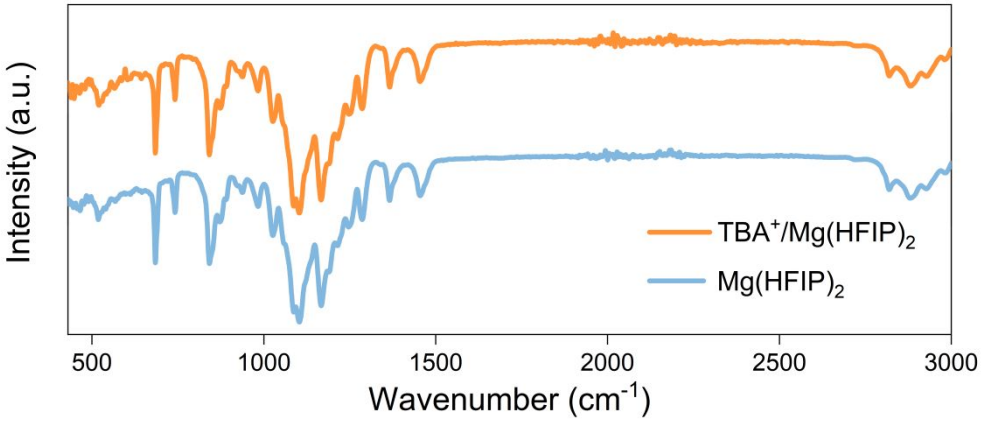

Figure S1. The FTIR spectra of $Mg(HFIP)_2$ and $TBA^+/Mg(HFIP)_2$ electrolyte.

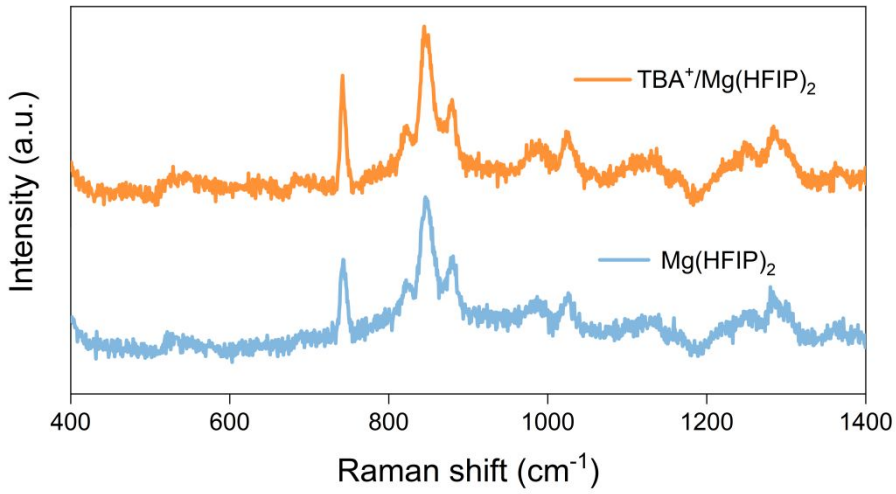

Figure S2. The Raman spectra of bulk $Mg(HFIP)_2$ and $TBA^+/Mg(HFIP)_2$ electrolyte.

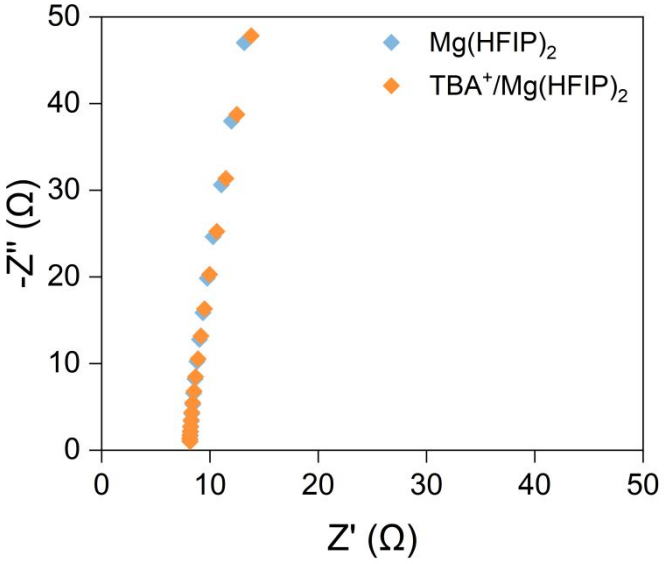

Figure S3. EIS of SS||SS symmetrical cells in $Mg(HFIP)_2$ and $TBA^+/Mg(HFIP)_2$ electrolytes.

The ionic conductivity (σ) of $Mg(HFIP)_2$ and $TBA^+/Mg(HFIP)_2$ electrolytes was calculated using Equation (1), where S denotes the effective contact area, R is the internal impedance of the cell, and L represents the separator thickness.

$$\sigma = \frac{L}{S \cdot R} \qquad (1)$$

From the EIS tests, the internal impedances were found to be 8.16Ω and 8.10Ω for $Mg(HFIP)_2$ and $TBA^+/Mg(HFIP)_2$ electrolytes, respectively. The calculated ionic conductivities are 3.07×10^{-4} S cm^{-1} and 3.05×10^{-4} S cm^{-1}.

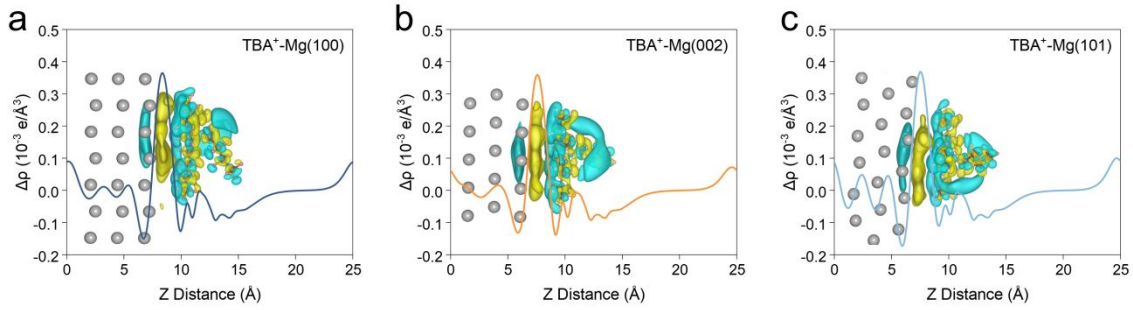

Figure S4. The surface-average electron density difference map for (a) Mg (100), (b) Mg (002), and (c) Mg (101) crystal planes in conjunction with TBA^+ cations.

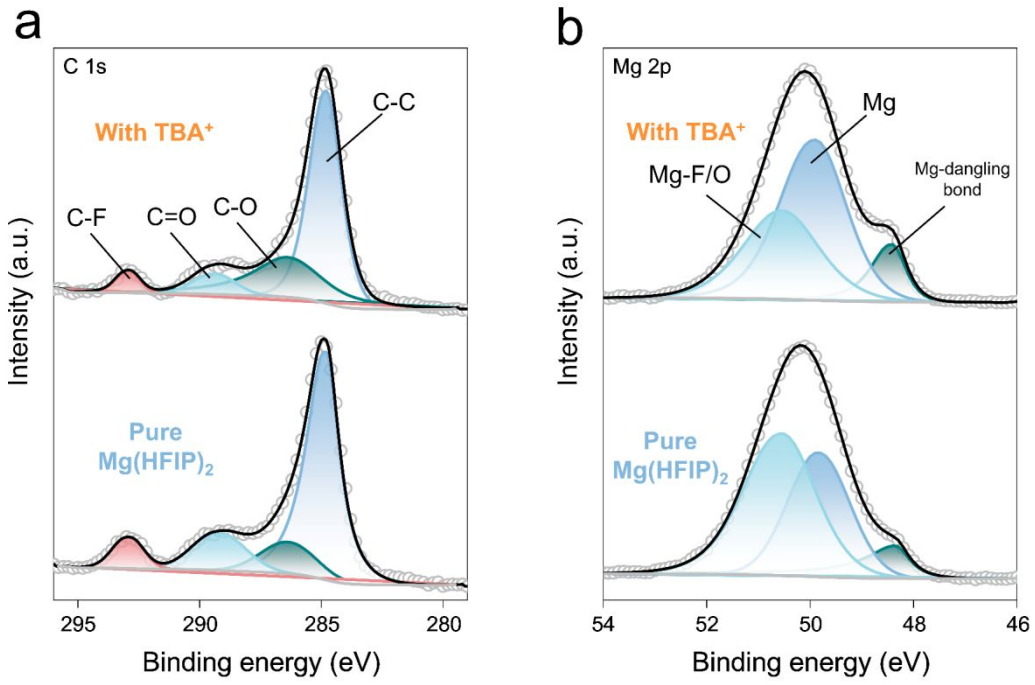

Figure S5. (a) C 1s and (b) Mg 2p XPS spectra of the cycled Mg metal in $Mg(HFIP)_2$ and $TBA^+/Mg(HFIP)_2$ electrolytes.

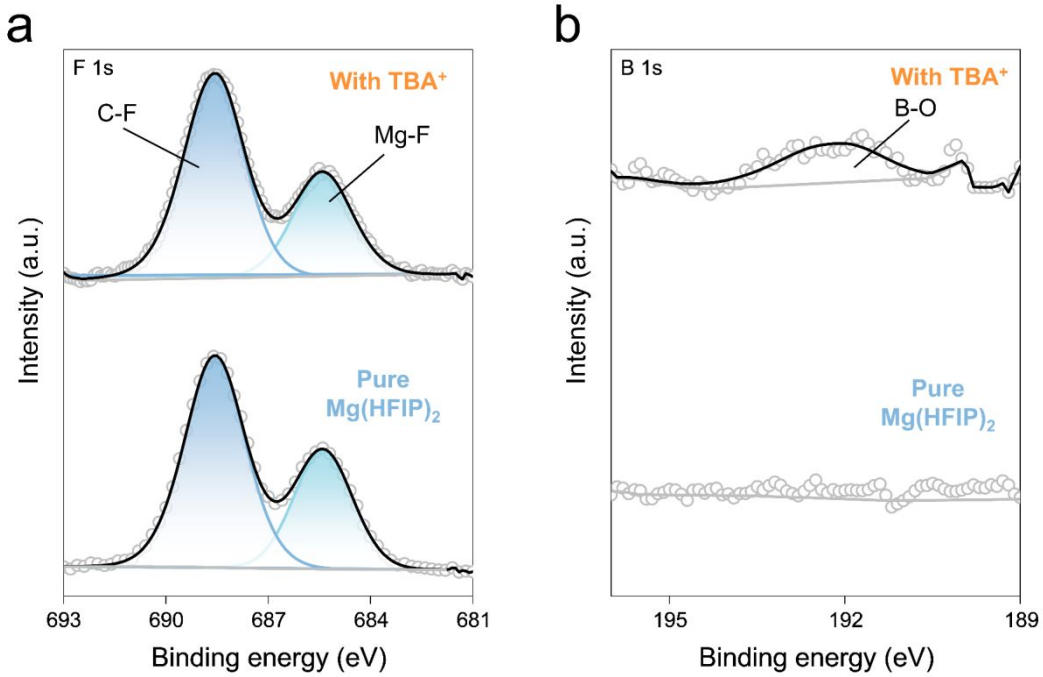

Figure S6. (a) F 1s and (b)B 1s XPS spectra of the cycled Mg metal in $Mg(HFIP)_2$ and $TBA^+/Mg(HFIP)_2$ electrolytes.

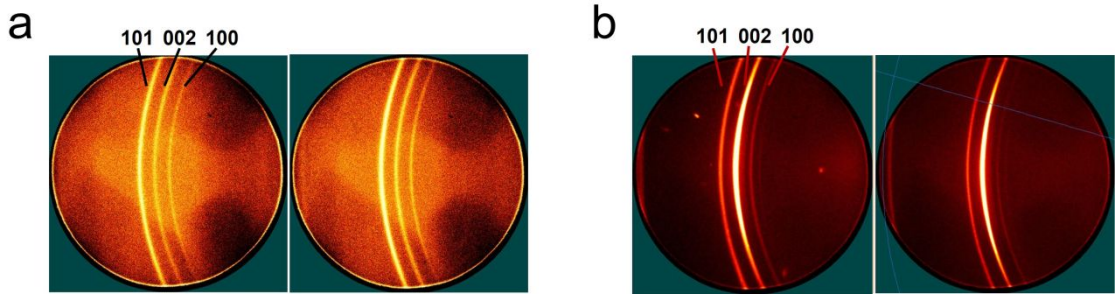

Figure S7. 2D WAXS results of Mg deposits in (a) $Mg(HFIP)_2$ electrolyte and (b) $TBA^+/Mg(HFIP)_2$ electrolyte.

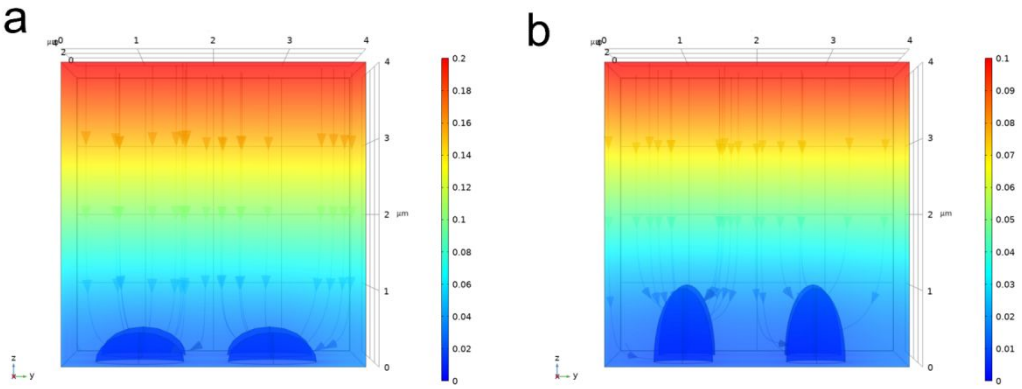

Figure S8. The simulation potential and current distribution of Mg deposition in $TBA^+/Mg(HFIP)_2$ and $Mg(HFIP)_2$ electrolytes.

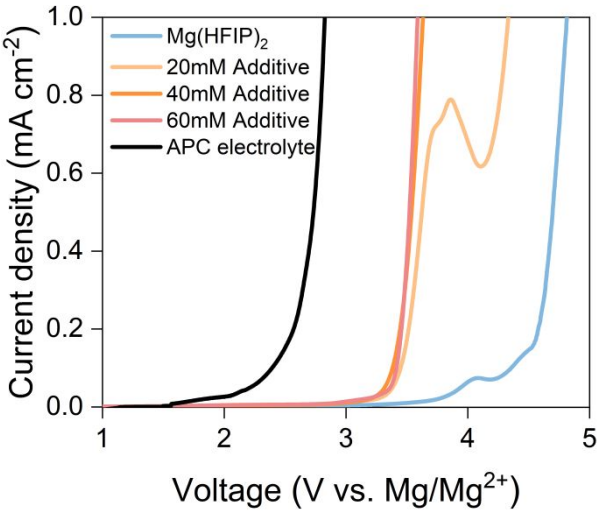

Figure S9. Oxidation stability of different electrolytes in stainless steel (SS) electrodes tested by linear sweep voltammetry.

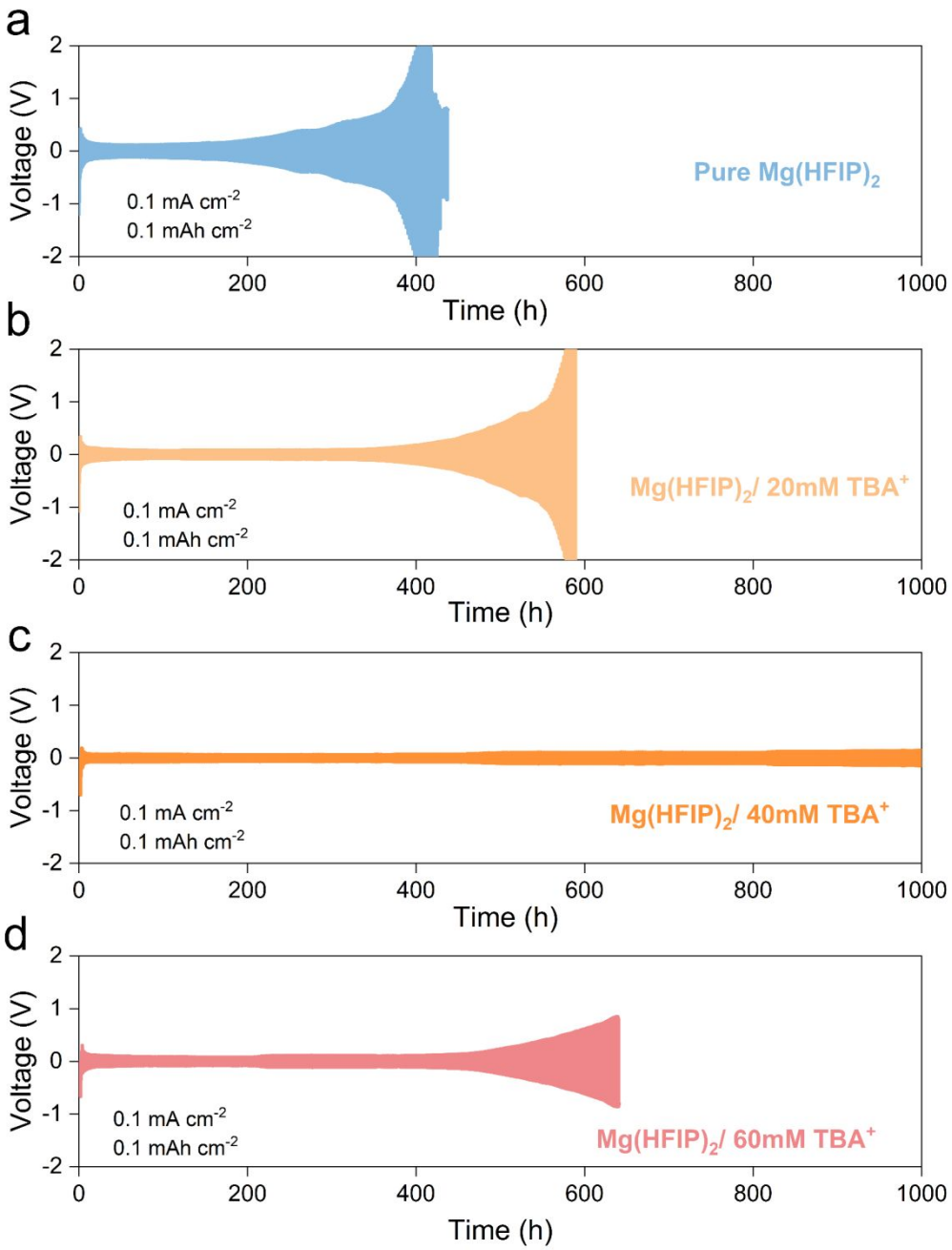

Figure S10. Overpotentials of Mg||Mg symmetric cells in $Mg(HFIP)_2$ electrolyte with different concertation additive at 0.1 mA cm^{-2} and 0.1 mAh cm^{-2}.

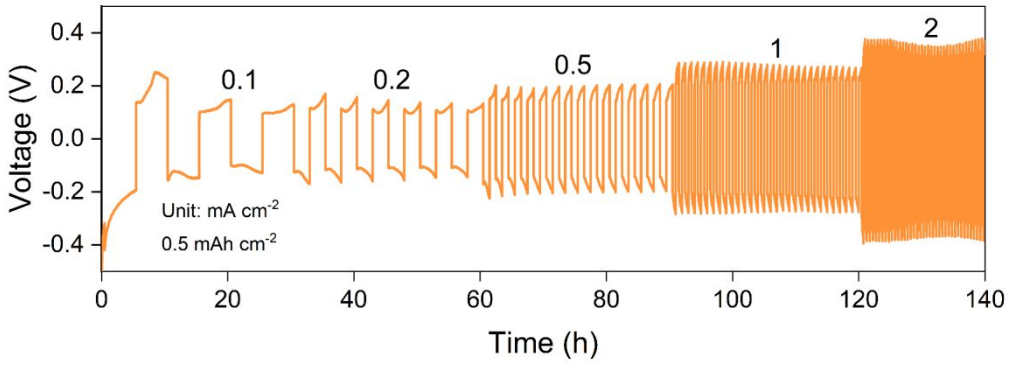

Figure S11. Overpotentials of Mg||Mg symmetric cells in $TBA^+/Mg(HFIP)_2$ electrolyte at various current densities from 0.1 to 2 mA cm^{-2} with a fixed capacity of 0.5 mAh cm^{-2}.

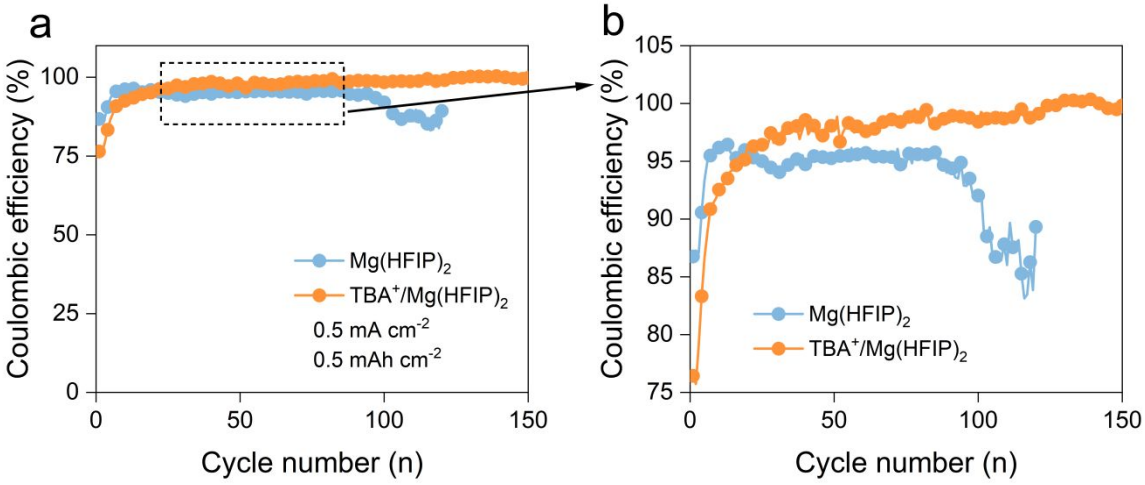

Figure S12. (a) Mg plating/stripping CEs in Mg||SS asymmetric cells using $Mg(HFIP)_2$ and $TBA^+/Mg(HFIP)_2$ electrolytes at 0.5 mA cm^{-2} and 0.5 mAh cm^{-2}. (b) An enlarged view of the CEs.

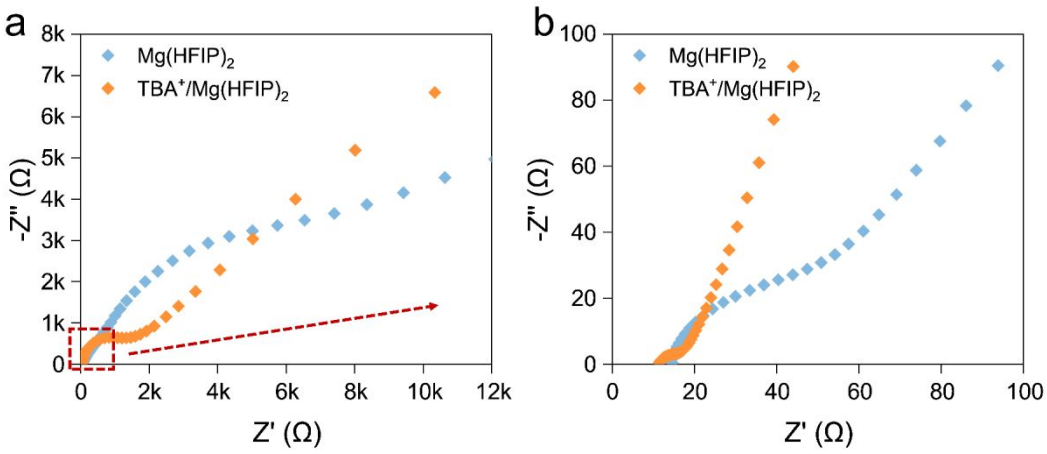

Figure S13. (a) EIS of cycled Mg||Mg symmetrical cells in $Mg(HFIP)_2$ and $TBA^+/Mg(HFIP)_2$ electrolytes. (b) An enlarged view of Nyquist plot which shows reduced internal resistance (R_S) and SEI resistance (R_{SEI}) (from 13.5 Ω to 11 Ω, 84 Ω to 13 Ω, respectively).

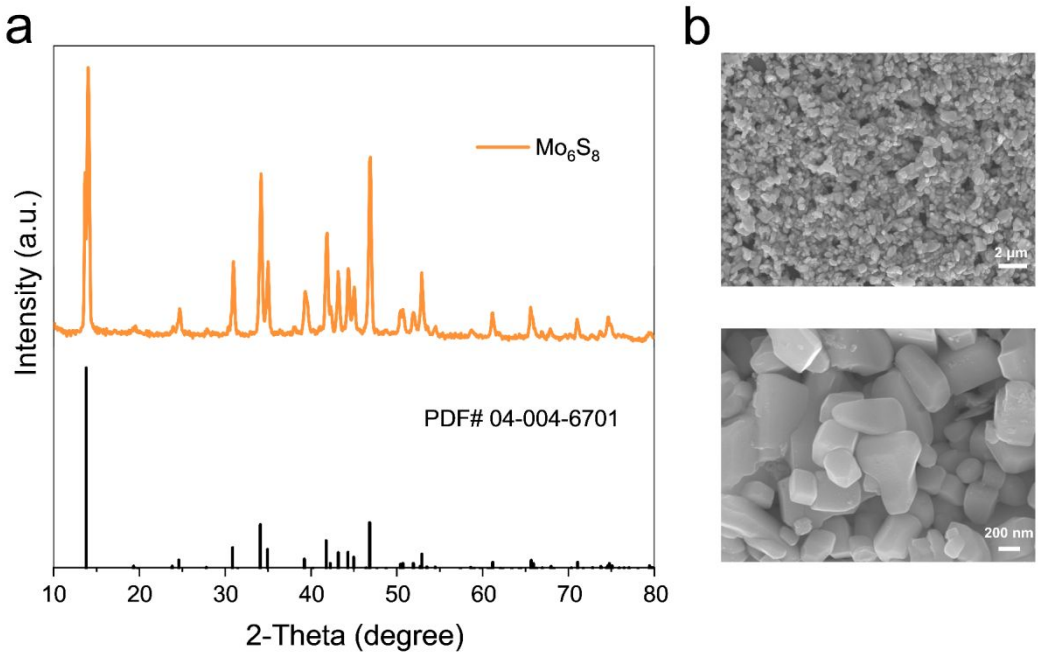

Figure S14. XRD pattern and SEM images of as prepared Mo_6S_8 cathode materials.

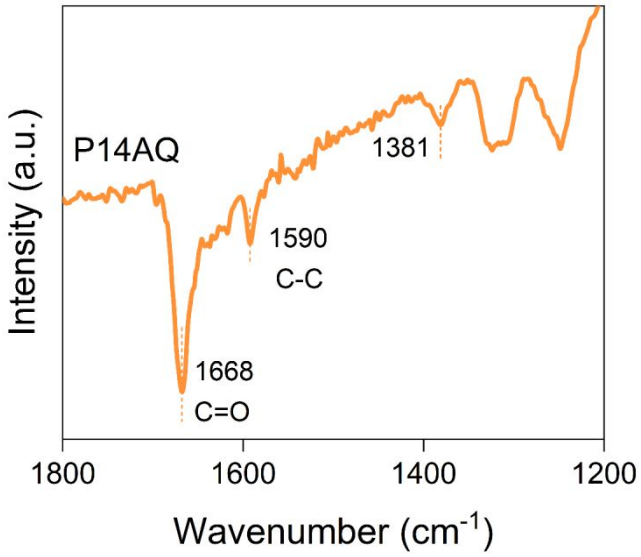

Figure S15. The FTIR spectra of as prepared P14AQ cathode materials.

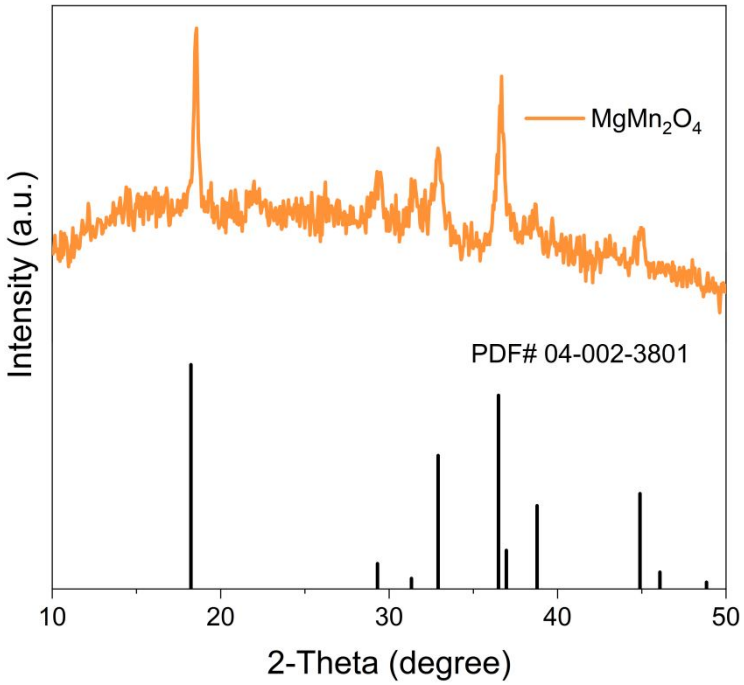

Figure S16. The XRD pattern of as prepared $MgMn_2O_4$ cathode materials.[7]

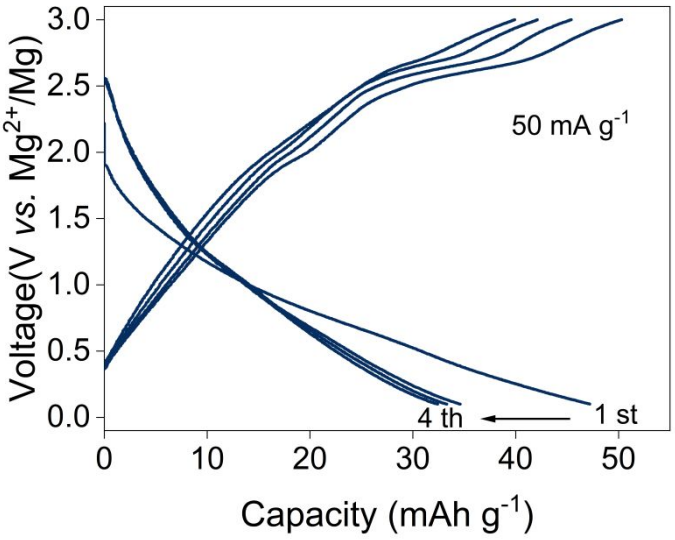

Figure S17. Charge−discharge curves of Mg||$MgMn_2O_4$ full cells at 50 mA g^{-1} in TBA^+/$Mg(HFIP)_2$ electrolyte.

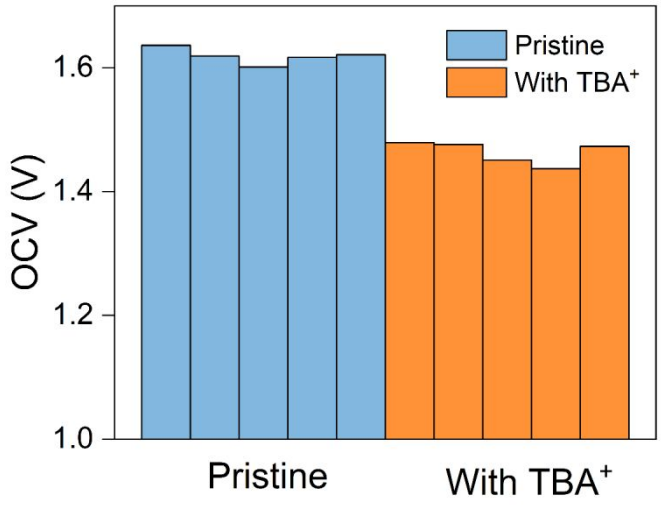

Figure S18. The open-circuit voltage (OCV) of Mg||Mo_6S_8 full cells with different electrolytes.

References

(1) Long, J.; Tan, S.; Wang, J.; Xiong, F.; Cui, L.; An, Q.; Mai, L. Revealing the Interfacial Chemistry of Fluoride Alkyl Magnesium Salts in Magnesium Metal Batteries. *Angew. Chem. Int. Ed.* **2023**, *62*, e202301934.

(2) Long, J.; Liu, Y.; He, Z.; Tan, S.; Xiong, F.; Xu, H.; Wang, W.; Zhang, G.; Yang, Z.; An, Q. Redesigning Solvation Structure toward Passivation-Free Magnesium Metal Batteries. *ACS Nano* **2024**, *18* (23), 15239-15248.

(3) Zhao-Karger, Z.; Xiu, Y.; Li, Z.; Reupert, A.; Smok, T.; Fichtner, M. Calcium-tin alloys as anodes for rechargeable non-aqueous calcium-ion batteries at room temperature. *Nat. Commun.* **2022**, *13*, 3849.

(4) Kresse, G.; Furthmüller, J. Efficient iterative schemes for ab initio total-energy calculations using a plane-wave basis set. *Phy. Rev. B* **1996**, *54* (16), 11169-11186.

(5) Grimme, S.; Ehrlich, S.; Goerigk, L. Effect of the damping function in dispersion corrected density functional theory. *J. Comput. Chem.* **2011**, *32* (7), 1456-1465.

(6) Momma, K.; Izumi, F. VESTA: a three-dimensional visualization system for electronic and structural analysis. *J. Appl. Crystallogr.* **2008**, *41* (3), 653-658.

(7) Truong, Q. D.; Kempaiah Devaraju, M.; Tran, P. D.; Gambe, Y.; Nayuki, K.; Sasaki, Y.; Honma, I. Unravelling the Surface Structure of MgMn2O4 Cathode Materials for Rechargeable Magnesium-Ion Battery. *Chem. Mater.* **2017**, 29 (15), 6245-6251.